Inorganic Chemistry

Article

pubs.acs.org/IC

Improper Ferroelectric Contributions in the Double Perovskite $Pb_2Mn_{0.6}Co_{0.4}WO_6$ System with a Collinear Magnetic Structure

Fabio Orlandi,*[,‡,†] Lara Righi,[†,∥] Francesco Mezzadri,[†,∥] Pascal Manuel,[‡] Dmitry D. Khalyavin,[‡] Davide Delmonte,[§,∥] Chiara Pernechele,[§] Riccardo Cabassi,[∥] Fulvio Bolzoni,[∥] Massimo Solzi,[§] and Gianluca Calestani[†,∥]

[†]Dipartimento di Chimica, Università di Parma, Parco Area delle Scienze 17/A, 43124 Parma, Italy

[‡]ISIS Pulsed Neutron Facility, STFC, Rutherford Appleton Laboratory, Chilton, Didcot, Oxfordshire OX11-0QX, United Kingdom

[§]Dipartimento di Fisica e Scienze della Terra, Università di Parma, Parco Area delle Scienze 7/A, 43124 Parma, Italy

[∥]IMEM-CNR, Parco Area delle Scienze 37/A, 43124 Parma, Italy

Supporting Information

ABSTRACT: The physical characterization and the extended crystallographic study of the double perovskite system $Pb_2Mn_{0.6}Co_{0.4}WO_6$ indicate an improper ferroelectric contribution to the polarization induced by the magnetic ordering. In the paramagnetic phase, the compound displays a centrosymmetric orthorhombic double perovskite structure with the *Pmcn1′* symmetry. The structure is strongly distorted by the lead stereoactivity. Magnetization measurements show two magnetic transitions at 188 and 9 K, but the time-of-flight neutron diffraction data provide evidence for a long-range magnetic ordering only below the second transition. Quantitative structure refinements combined with a comprehensive symmetry analysis indicate the $Pm'c2_1'$ magnetic space group to be the adequate symmetry to describe the structural distortions and spin ordering in the ground state of the system. The symmetry implies a coexistence of a spontaneous ferromagnetic moment and a ferroelectric polarization along the orthogonal ***b***- and ***c***-axes, respectively, in the long-range ordered structure. Macroscopic measurements confirm the presence of the spontaneous polarization also below the first transition at 188 K, where only short-range magnetic correlations are evidenced by diffuse scattering in neutron diffraction.

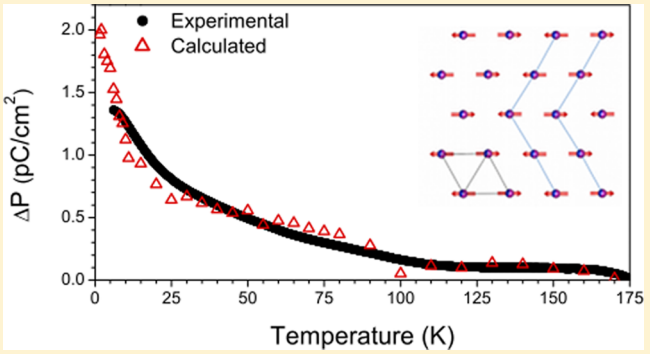

INTRODUCTION

In recent years, many efforts have been devoted to the study of multifunctional materials in order to obtain new devices that can handle several tasks. In this context, the magneto-electric multiferroics hold a special place. These materials are generally classified on the basis of the relationship between the ferroic properties.[1] In type I multiferroics, the electric and magnetic ferroic orders have different microscopic origin. In particular, these materials are proper ferroelectrics in which the polarization is induced by an off-centering of the cations in the oxygen coordination polyhedra. This ferroelectric distortion can be driven by a second order Jahn−Teller effect[2] that confers a covalent character to the bonds between the cation and the oxygen atoms. The perovskite oxides, with general formula ABO_3, are one of the most common examples.[2,3] In these compounds, the ferroelectric distortion is usually determined by a d^0 metal on the B site,[2] or alternatively by the stereoactive role of a lone pair ion like Pb^{2+} or Bi^{3+} in the A site.[3] Type II multiferroics are improper ferroelectrics, in which the spontaneous polarization is induced by the magnetic order; this often implies a strong magnetoelectric coupling but the spontaneous electric polarization usually assumes small values unsuitable for applicative purposes.[4,5] From a crystallographic perspective, the breaking of time inversion symmetry and the suppression of the inversion center are simultaneously required in order to allow the occurrence of both spontaneous magnetic and electric polarizations. Normally, the symmetry reduction at the onset of the long-range magnetic order can be considered the evidence of a spin driven Jahn−Teller (SDJT) mechanism first shown by Yamashita and Ueda[6] in pyrochlore systems. There are additional examples of SDJT effects reported in the literature on both collinear and noncollinear magnetic systems.[6−16] In the case of a collinear structure, the orthorhombic rare earth manganites $RMnO_3$ (R = Ho, Y) represent one of the first documented examples.[7] These systems show incommensurate magnetic ordering below $T_{N1} \approx 42$ K; at $T_{N2} \approx 26$ K the propagation vector locks into a commensurate value, giving rise to an E-type antiferromagnetic (AF) structure.[7] Pyrocurrent measurements reveal, in con-

Received: January 15, 2016
Published: April 14, 2016

DOI: 10.1021/acs.inorgchem.6b00117
Inorg. Chem. 2016, 55, 4381−4390

junction with T_{N2}, the appearance of electrical polarization.[7] Sergienko et al.,[8] using the Landau theory, showed that the E-type AF ordering could break the spatial inversion center promoting a spontaneous polarization. The polarization experimentally observed was 0.008 $\mu C/cm^2$ and 0.15 $\mu C/cm^2$ in a polycrystalline sample[7] and in a single crystal, respectively,[9] well below the outstanding calculated values ranging between 0.5 and 12 $\mu C/cm^2$.[8] Further examples are represented by the series RMn_2O_5 with R = rare earth. These compounds order magnetically below 50 K with an incommensurate propagation vector that depends on the ionic radii of the rare earth.[10] By decreasing the temperature, the propagation vector locks to a commensurate periodicity and the magnetic structure results in an almost collinear AF structure. It was pointed out that the system shows large variations of the dielectric properties in conjunction with all these magnetic transitions, in particular, at the occurrence of the commensurate phase.[10] Moreover, clear evidence of magneto-electric coupling, indicating strong spin−lattice interactions were observed, such as reversal of the electrical polarization by the application of a magnetic field[12] and colossal magneto-dielectric effect.[13]

The double perovskite structure, $A_2BB'O_6$, represents an interesting playground to study the interactions between the ferroic orders. The possibility to select B/B′ couples of cations allows the tailoring of the physical properties and the eventual promotion of new forms of coupling between ferroic orders. Moreover, by placing a stereoactive cation like Pb^{2+} or Bi^{3+} in the A site it is possible to induce lattice distortions which can contribute to the occurrence of (anti)-ferroelectric ordering as well as frustrated magnetic interactions.

In this paper, we present a new double perovskite compound $Pb_2Mn_{0.6}Co_{0.4}WO_6$ (PMCW) showing magnetically driven ferroelectric contributions below 188 K. This compound, like the solid solution end member Pb_2MnWO_6,[17] shows an orthorhombic double perovskite structure with huge lattice distortion due to the strong stereoactivity of the lead atom. Indeed, the substitution of Mn^{2+} with Co^{2+} induces an increase of the magnetic transition temperature up to 188 K indicating a change in the magnetic interactions of the system. In this work, the complete structural characterization of the system in conjunction with a comprehensive electrical and magnetic characterization is presented. Time of flight neutron diffraction experiments and careful symmetry analysis demonstrate the breaking of both time and spatial inversion symmetries providing an explanation for the presence of an induced ferroelectric state experimentally measured below the magnetic transition.

EXPERIMENTAL SECTION

The PMCW compound was synthesized by solid-state reaction. Stoichiometric amounts of PbO, $MnCO_3$, CoO, and WO_3, with 50/50 ratio between Co and Mn, were grounded and fired at 850 °C for 2 h in Ar atmosphere. The obtained powder was reground, pressed into pellet and sintered at 850 °C for 6 h in Ar atmosphere. The phase purity was checked by means of Powder X-ray Diffraction (PXRD) analysis performed on a Thermo ARL X'tra diffractometer with Cu Kα radiation and equipped with a Si(Li) solid-state detector able to cut off the fluorescence contribution due to manganese and cobalt. Temperature-dependent patterns were collected on the same diffractometer by using an Anton Paar TTK-450 chamber in the temperature range RT−400 K. Synchrotron diffraction data (SPXRD) were collected at RT on the ID15B beamline at the ESRF institute (Grenoble), using hard X-ray radiation with λ = 0.142 Å.

Time of Flight neutron diffraction (ToF-NPD) experiments were carried out at the ISIS facility (U.K.) on the WISH instrument.[18] The diffraction data were collected on powdered samples, using a thin vanadium sample holder, in the 1.5 K−RT temperature range. The nuclear and magnetic structure refinements were carried out with the Jana2006 software,[19] the magnetic symmetry analysis was performed with the help of the ISODISTORT software.[20]

Zero field cooling (ZFC) and Field Cooling (FC) magnetization measurements were performed, with different applied fields, on a sintered pellet by means of a SQuID MPMS XL Quantum Design magnetometer. Magnetization hysteresis loops were measured at different temperatures in the field range ±5 T.

The DC electrical resistivity ρ was measured with a two contacts configuration in the temperature range 5−300 K. The dielectric constant was measured eliminating contact effects as shown in ref 21, with a LCR meter HP4824A covering the frequency range from 20 Hz to 1 MHz, applying a sinusoidal signal of 50 mV. Pyroelectric currents were measured on a metalized pellet. The poling of the sample was obtained by using a Keithley 2400 Source Meter Unit, and a Keithley electrometer 6517B was adopted to detect the electric current. The measurement of the ferroelectric hysteresis loop was carried out at RT and 77 K by means of AIXACCT TF-Analyzer 2000E ferroelectric tester. The sample was lapped and metalized with a 20 nm layer of platinum by sputtering technique approximating a parallel plate capacitor, with thickness of t = 350 μm and area of A = 5 mm^2.

RESULT AND DISCUSSION

Crystal Structure Characterization. The PXRD pattern of PMCW can be indexed with a perovskite superstructure related to the simple perovskite by the relations $\boldsymbol{a} \approx 2\boldsymbol{a}_p$, $\boldsymbol{b} \approx \sqrt{2}\boldsymbol{a}_p$, and $\boldsymbol{c} \approx 2\sqrt{2}\boldsymbol{a}_p$ ($\boldsymbol{a}_p \approx 3.8$ Å); a minor impurity phase, present at 4.5% in weight, was detected and identified as lead tungstate $PbWO_4$. The crystal structure at room temperature (RT) was solved and refined from SPXRD data collected at the ID15B beamline and from ToF-NPD data collected at WISH.[18] The best solution was found in the centrosymmetric *Pmcn1′* space group (we indicate the magnetic space group in the Belov−Neronova−Smirnova notation (BNS) and the non magnetic phase with the corresponding gray group). The refinement in the noncentrosymmetric $Pmc2_11'$ space group, characteristic of the Pb_2MnWO_6 compound,[17] did not improve the fit and the reliability factors despite the increase of the refinable parameters. The RT structure was refined simultaneously on the WISH instrument banks with 2θ = 152.8°, 121.6°, 90° and on the ID15B SPXRD. The Rietveld plots of the 90° NPD data of WISH and of the SPXRD data are reported in Figure 1, and corresponding crystal data together with the reliability factors are listed in Table 1. Further details on the structural refinements based on the additional WISH banks are inserted in the Supporting Information.

The refined structure represents the classical prototype of an ordered orthorhombic double perovskite, like Pb_2MgWO_6.[22] The B site results completely ordered in a NaCl-type arrangement. Despite this, the occupancy of the Mn/Co site deviates significantly from the expected 0.5/0.5 values, indicating that the obtained phase is Mn-rich and its chemical formula, based on the diffraction data, can be expressed as $Pb_2Mn_{0.6}Co_{0.4}WO_6$. The missing cobalt is likely enclosed in the lead tungstate impurity, but the presence of a small amount of CoO, not detectable by diffraction measurement, cannot be excluded. The refined average bond lengths are in agreement with the expected values for the Pb^{2+} and W^{6+} ions, as well as for Co^{2+} and Mn^{2+} in high spin (hs) configuration (see Figure 2). Selected angles and bond lengths are reported in Table S-2. Charge distribution analysis performed with the CHARDIS99

DOI: 10.1021/acs.inorgchem.6b00117
Inorg. Chem. 2016, 55, 4381−4390

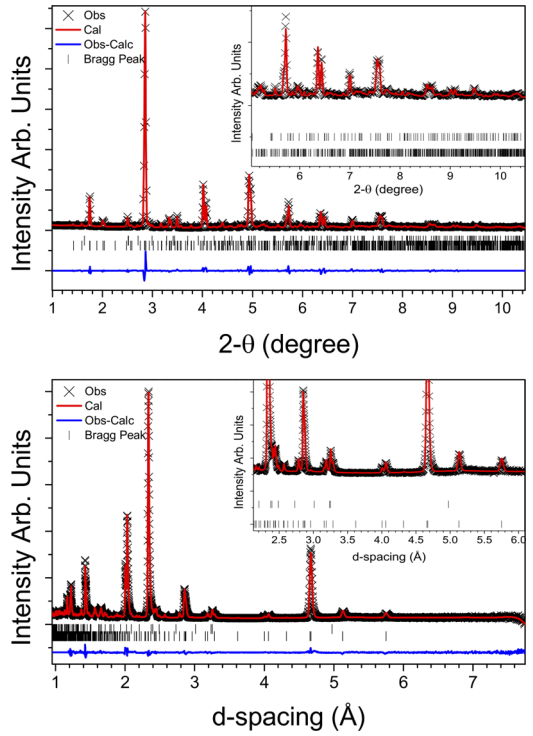

Figure 1. Rietveld plots of PMCW: SPXRD data (top) and 90° bank of the WISH beamline (bottom). Observed (× , black), calculated (line, red), and difference (bottom line, blue) patterns are reported. Upper tick marks indicate the Bragg positions of the lead tungstate impurity, and the lower tick marks the ones of the main phase.

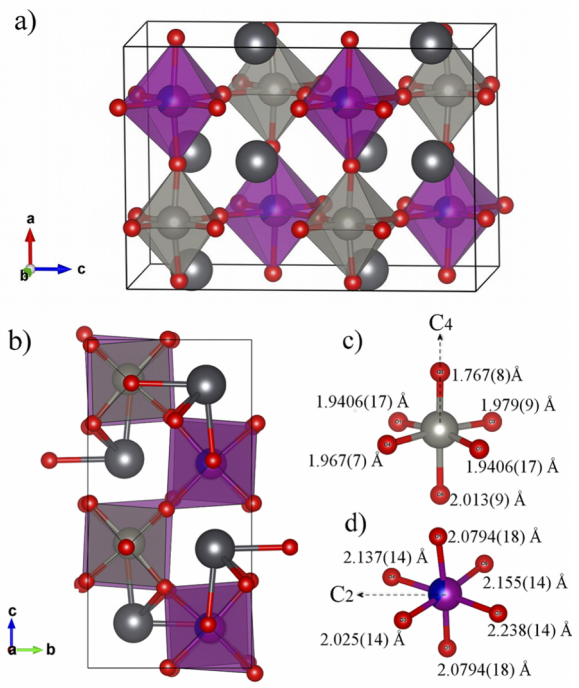

Figure 2. a) PMCW crystal structure at room temperature: black and red spheres represent lead and oxygen atoms, respectively, whereas tungsten and manganese/cobalt coordination octahedra are indicated in gray and violet. b) Projection of the structure on the ***bc*** plane, highlighting the four short Pb—O bonds. c), d) Graphical representation of the distorted octahedra of the tungsten (gray) and cobalt/manganese (blue/violet) atoms; the arrows indicate the direction of the local rotation pseudoaxis preserved in the distortion.

software[23] returns reliable bond valence sum values for the cations in the system, in particular 2.02 for the Mn/Co site, 5.93 for W and 2.03 for Pb.

Although distorted by the stereoactivity of the lead atoms, the BO_6 octahedral framework does not show evident tilting. The asymmetric coordination of the lead atoms, resulting in four short bonds (ranging from 2.571(5) to 2.672(3) Å) opposite to the lone pair,[24] is reported Figure 2b. The WO_6 polyhedra present a distortion typical of the d^0 cations, characteristic for example of Ti^{4+} in the tetragonal phase of $PbTiO_3$.[25] The distortion, showing a pseudo C_4 type symmetry,[26] consists of four almost equal basal bonds, ranging from 1.9406(17) to 1.979(9) Å, and in two apical bonds, one elongated (2.013(9) Å) and the other remarkably shortened (1.767(8) Å) as drawn in Figure 2c. The magnitude of the WO_6 distortion, calculated according to ref 26, can be considered weak (Δd = 0.25 Å) and is notably smaller than that of Pb_2MnWO_6 at the same temperature.[17] This may indicate that the isovalent substitution of Mn^{2+} with Co^{2+} determines the relaxation of the WO_6 distortion. The Mn/Co octahedron is less distorted (Δd = 0.22 Å) with respect to the tungsten one, but presents a pseudo-C_2 type of distortion,[26] moving from the center to an edge of the octahedron, as indicated in Figure 2d. The atomic displacement parameters (ADPs) of the oxygen atoms are relatively high if compared to those of the remaining atomic sites; this is basically due to the static disorder accounted by considering the statistical composition of the Mn/Co site. Indeed, the different ionic radii of the two cations

Table 1. Crystal Data and Refinement Reliability Factors for PMCW

	chemical formula			$Pb_2Mn_{0.6}Co_{0.4}WO_6$	
	Z			4	
	space group			*Pmcn1′*	
	a (Å)			8.01546(8)	
	b (Å)			5.73574(8)	
	c (Å)			11.51064(18)	
	volume (Å^3)			529.197(12)	
	d (g cm^{-3})			9.42	
	WISH2 θ = 152.8°	WISH2 θ = 121.6°	WISH2 θ = 90.0°	SPXRD λ = 0.142 Å	overall
GoF	2.46	2.76	2.46	3.99	2.93
R (F_{obs})	3.27	2.77	3.22	3.91	
R_p	3.61	3.40	3.61	5.30	5.11
R_{wp}	4.66	4.23	3.96	7.11	4.61

DOI: 10.1021/acs.inorgchem.6b00117
Inorg. Chem. 2016, 55, 4381−4390

(Mn^{2+} = 0.83 Å and Co^{2+} = 0.74 Å), lead to the expected local disordering of oxygen positions.

By decreasing the temperature below RT, no evident structural transition was detected in the ToF-NPD data. In Figure 3, the thermal evolution of the cell parameters as a function of temperature is shown. Whereas the thermal behavior of the ***a***-axis can be described by a typical phonon activated evolution, the ***b***- and ***c***-axes increase from RT to 200 K, and down to 2 K the two unit cell constants stabilize and no further detectable changes are observed. Below 30 K two additional anomalies, underlined in the inset of Figure 3 with T_{A1} and T_{A2}, in the cell constants and volume are revealed by NPD measurements. The evolution of the bond lengths with temperature are reported and discussed in the SI.

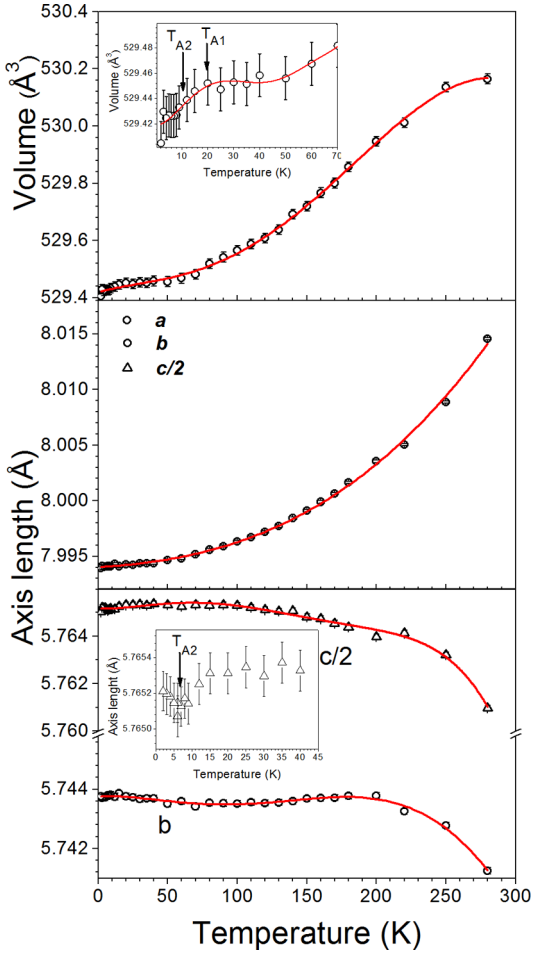

Figure 3. Thermal evolutions of lattice parameters and cell volume of PMCW. Top: cell volume. A zoom of the low temperature region showing two anomalies at T_{A1} and T_{A2} is shown in the inset. Middle: ***a***-axis. Bottom: ***b***-axis compared with ***c***/2. A zoom of the low temperature region, pointing out an anomaly for ***c***/2, is reported in the inset. In all cases, the error bars are smaller than the symbol size and the red line only represents a guide for the eyes.

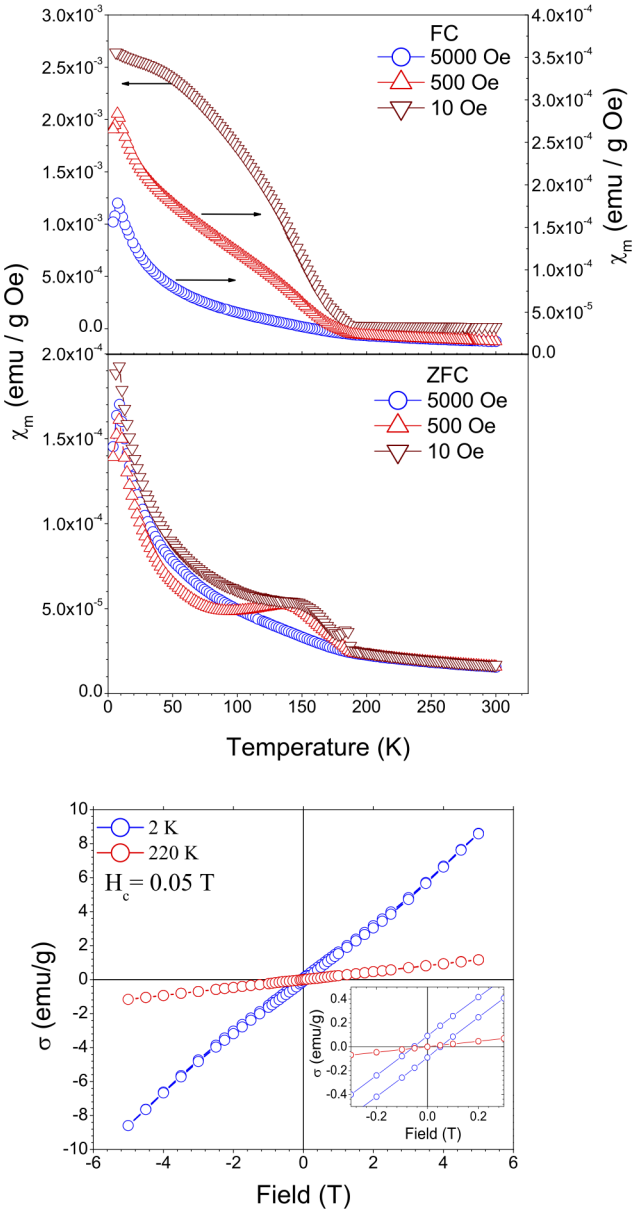

Figure 4. Field dependence of the FC and ZFC magnetization curves (top) measured at different applied field; the FC curves at 500 (up triangles) and 5000 (circles) Oe refer to the right axis. Bottom: hysteresis loops measured at 220 and 2 K; as shown in the inset, a small coercive field H_C = 0.05 T is observed at 2 K.

Magnetic and Electrical Characterizations. The magnetization measurements, shown in Figure 4, display a first magnetic transition at T_{C1} = 188 K, strongly influenced by the applied field. By decreasing the temperature, a second magnetic transition, showing the characteristic cusp at the onset of antiferromagnetic order, is detected around T_{C2} = 9 K. Despite this, the irreversibility between ZFC and FC measurements observed for low applied field is consistent with weak ferromagnetic contributions. With the increase of the applied field the ZFC and FC curves tend to superimpose (see Figure S-3), and the complete overlay is achieved for H_a > 5000 Oe. Simultaneously, the reduction of the susceptibility, particularly evident in the FC measurements, is observed in association with the disappearing of the first transition at T_{C1}. This type of behavior is observed in different double perovskites containing Mn^{2+} or Co^{2+} with diamagnetic atoms in the B′ site, where these features are ascribed to the presence of point and line defects or short-range magnetic ordering.[17,27−30] It is noteworthy that, with respect to Pb_2MnWO_6,[17,30] the highest magnetic transition temperature is increased up to 188 K, suggesting that it could be strongly related to the presence of Mn—O—Co interactions. In the present case, as for

DOI: 10.1021/acs.inorgchem.6b00117
Inorg. Chem. 2016, 55, 4381−4390

Pb_2MnWO_6,[17,30] the crystallographic characterization indicates the absence, at least within the resolution of our data, of antisite defects. This leads us to conclude that the transition observed at T_{C1} could be related to antiphase boundary (APB) defects, generated at the grain boundary between two crystal domains with opposite B and B′ arrangements. These defects are quite common in double perovskite compounds and are responsible for the occurrence of B—O—B interactions.

Figure 4 (bottom) shows the hysteresis loops of the sample measured in the ±5 T field range at 220 and 2 K. The small coercive field observed at 2 K (H_C = 0.05 T) is consistent with a weak ferromagnetism, as hypothesized on the basis of the $M(T)$ measurements; furthermore the predominant linear character and the absence of saturation are indication of an AF nature of the sample.

Focusing on the electrical properties, the sample is insulating in the 4−400 K temperature range with high values of the dielectric constant; detailed analysis of the measurements are reported in the SI. Pyroelectric measurements were performed on the same sample used for the resistivity characterizations and reported in Figure 5. The curve shows a complex behavior of the DC polarization in the sample with the presence of two peaks, denoted as T_1 and T_2 and occurring around 200 and 15 K, respectively.

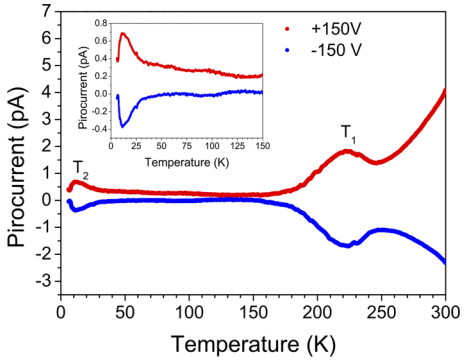

Figure 5. Pyrocurrent measurements of the PMCW sample: typical pyrocurrent profile after poling with voltage V = ± 150 V.

The first peak around T_1 = 200 K is likely related to the weak ferromagnetic transition observed in the magnetization measurement at T_{C1}, whereas the second pyrocurrent peak detected at 10 K, see inset Figure 5, is related to the antiferromagnetic transition at T_{C2}. These effects joined with the information provided by magnetic measurements, represent an indication of a possible spin−lattice coupling in this system. Furthermore, the inversion of the pyrocurrent peaks with the change of the poling field sign indicates a possible ferroelectric character of these contributions. Indeed, Figure 6 shows the ferroelectric hysteresis loop of the $Pb_2Mn_{0.6}Co_{0.4}WO_6$ compound obtained at 77 K with a Dynamic Hysteresis Measurement (DHM). This type of measurement consists in two triangular prepulses (positive and negative) which guide the system electric dipoles orientation; the current is measured under the application of subsequent triangular AC voltage signals of the same amplitude and frequency and integrated in order to obtain the polarization. The loop was obtained after the subtraction of the voltage-invariant displacement current contribution of the sample, and the saturation is not reached within the available fields range. At RT, it was not possible to detect any hysteresis loop as can be observed in Figure 6 (blue

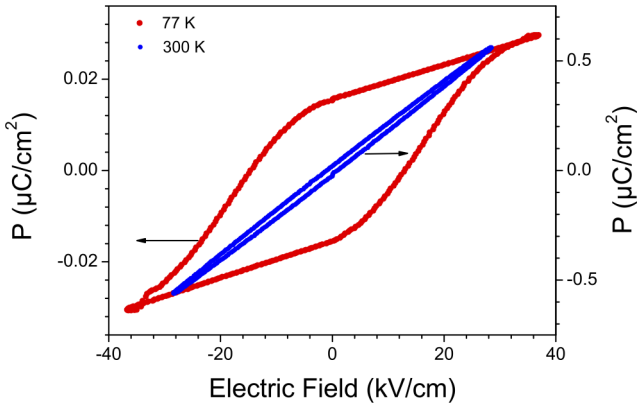

Figure 6. Ferroelectric hysteresis loop of the $Pb_2Mn_{0.6}Co_{0.4}WO_6$ measured with the DHM protocol at RT and 500 Hz (blue point, right axis) and at 77 K and 800 Hz (red point, left axis). The trend of the RT measurement is typical of a paraelectric material with small leakage.

curves), where the polarization highlights an almost linear dependence on the applied voltage superimposed with very low leakage contributions. Therefore, T_{C1} may be denoted as the para-to-ferroelectric transition temperature. The value of the remnant polarization at 77 K is small, indicating a possible improper ferroelectric state; at the same time the quite high coercive electric field (i.e., 11.5 kV/cm) denote hard characteristics.

Magnetic Structure Analysis. A series of ToF-NPD experiments were performed on the WISH instrument in the temperature range 1.5−300 K. Some extra reflections, having the characteristic temperature and form factor dependence of magnetic reflections (Figure 7), appear below 9 K, differently from what happens at the first magnetic transition (T_{C1} = 188 K), below which only an increase of diffuse scattering in the d-range 7−12 Å is observed. This diffuse scattering becomes particularly evident below 80 K (see inset of Figure 7 and Figure S-6) which, in conjunction with a strong temperature dependence of the paramagnetic background, is indicative of changes in the magnetic interactions. To better analyze the evolution below T_{C1}, the background on the long-d bank (2θ = 27.0°) was integrated in the d-range 14−18 Å above any trace of diffuse scattering, and plotted in the bottom of Figure 7. The integrated value decreases monotonically from 190 K down to the lowest temperature as indication of a progressive increase of the magnetic interactions (the anomaly around 90 K is an artifact due to a change in the operation of the cryostat). This is confirmed also by the conservation of the total scattering across T_{C1} (see Figure S-7), obtained in the q-range 0.25−13 $Å^{-1}$ as done in ref 31. As described above, the origin of the high temperature transition may be ascribed to APB's possessing a limited spatial distribution compatible with the observed diffuse scattering.[17,27−30] In the case of PMCW, three interactions are present in the APBs, namely Mn—O—Mn, Co—O—Co, and Mn—O—Co. The different characteristic temperatures of these interactions can account for the complex thermal behavior of the paramagnetic background and of the diffuse scattering as well.

From the analysis of the diffraction pattern collected at 1.5 K, it is evident that the propagation vector κ_1 = (0 0 0), implying the presence of magnetic intensity on the nuclear reflections, is not sufficient to index the whole magnetic pattern. By using the k-search software[32] of the Fullprof suite, it was possible to index

DOI: 10.1021/acs.inorgchem.6b00117
Inorg. Chem. 2016, 55, 4381−4390

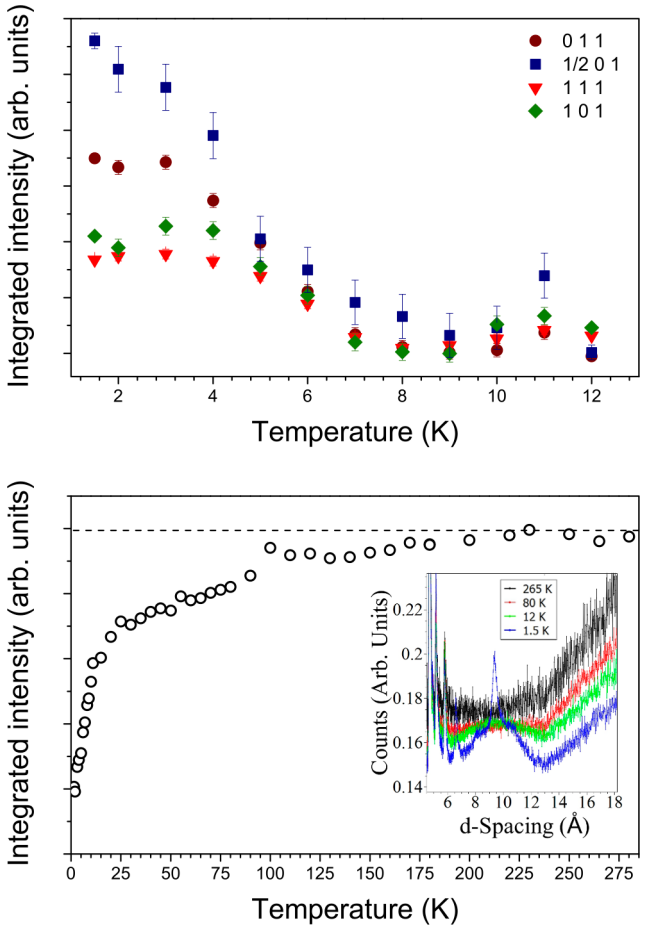

Figure 7. Top: intensity of selected magnetic reflections as a function of the temperature; the indices refer to the nuclear unit cell. Bottom: integration of the paramagnetic background in the *d*-range 14−18 Å as a function of the temperature, the dashed line indicates the value of the integrated background at RT. The inset reports the neutron diffraction data for the high *d*-spacing region underlining the rise of the diffuse scattering lowering the temperature.

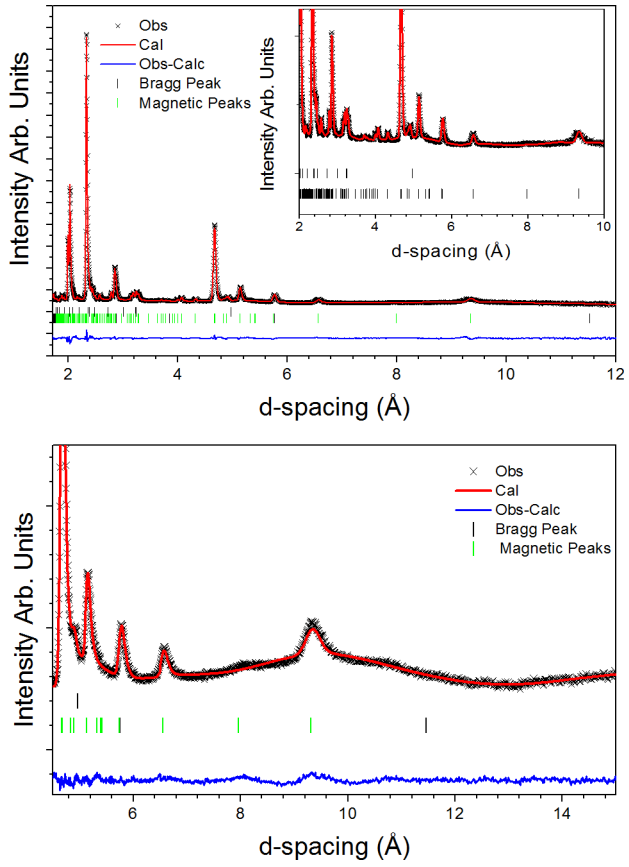

Figure 8. Rietveld plot of the WISH banks with 2θ = 58.3° and 27.0° of the $Pm'c2_1'$ model at 1.5 K; the zoom of the high d-space region of the 2θ = 58.3° bank is shown in the inset. Observed (× , black), calculated (line, red), and difference (bottom line, blue) patterns are reported. Upper tick marks indicate the Bragg positions of the lead tungstate impurity, and the lower tick marks the ones of the main phase, green tick marks indicate the magnetic Bragg reflections.

the remaining peaks with a propagation vector κ_2 = (1/2 0 0). The magnetic symmetry was analyzed by means of the ISODISTORT[20] software combining the two propagation vectors κ_1 and κ_2; the output of the analysis is reported in Table S-3. An accurate analysis of the magnetic systematic absences was performed with the help of the MAGNEXT[33] software of the Bilbao crystallographic server,[34−36] in order to reduce the number of the possible magnetic space groups.

The quantitative Rietveld refinement was performed in all the possible magnetic space groups having the appropriate systematic extinctions. The best agreement between observed data and the calculated model was obtained for the $Pm'c2_1'$ magnetic space group (referring to a new magnetic cell with basis = {(2,0,0),(0,1,0),(0,0,1)} and origin shift = (3/4,1/4,0) with respect to the nuclear one). This symmetry is a result of a common action of the two magnetic irreducible order parameters; one-dimensional mGM2+/mGM4−(ξ) and two-dimensional mY2($\eta_1 \neq 0$, $\eta_2 = 0$) associated with κ_1 = (0 0 0) and κ_2 = (1/2 0 0), respectively. Both combinations mGM2+⊕ mY2 and mGM4−⊕ mY2 result in the same magnetic space group $Pm'c2_1'$, and the proposed magnetic structure implies admixture of mGM2+ and mGM4− with equal amplitudes to keep constant moments on the Mn/Co sites. The corresponding Rietveld plots, of selected banks, are reported in Figure 8, the results of the refinement are summarized in Table 2, whereas the atomic coordinates of the magnetic cell and the additional Rietveld plots are reported in the SI. Besides the symmetry constraints imposed by the magnetic space group, further constraints were imposed during the last steps of the refinement, as suggested by the behavior of some parameters on achieving the convergence. In particular, the M_z moduli of the three independent Mn/Co sites, approaching similar values during refinement, were constrained to be equal. Similarly, M_x (for the Mn/Co1 site) and M_y, assuming negligible values within the e.s.d.'s, were fixed to zero.

The refined values of the magnetic parameters are reported in Table 3. The small value of the refined magnetic moment with respect to the expected one (~4 μ_B in case of Mn^{2+} *hs* and Co^{2+} *hs* with unquenched orbital momentum) is probably due to the chemical disorder of the magnetic site. Moreover, from Figure 8, the presence of diffuse scattering is evident even at 1.5 K, indicating the presence of short-range interactions possibly generated by the not fully relieved frustration of the magnetic ordering in the system.

The refined magnetic model, consisting of a collinear antiferromagnetic structure with the spins lying along the *c* direction, is reported in Figure 9. The "fundamental unit" of the

DOI: 10.1021/acs.inorgchem.6b00117
Inorg. Chem. 2016, 55, 4381−4390

Table 2. Crystal Data and Refinement Reliability Factor at 1.5 K

chemical formula			$Pb_2Mn_{0.6}Co_{0.4}WO_6$			
magnetic space group			$Pm'c2_1'$			
a (Å)			15.9836(5)			
b (Å)			5.7421(2)			
c (Å)			11.5272(4)			
volume (Å^3)			1057.98(6)			
κ_1			(0 0 0)			
κ_2			(1/2 0 0)			
	WISH 2θ = 152.82°	WISH 2θ = 121.66°	WISH 2θ = 90°	WISH 2θ= 58.33°	WISH 2θ = 27.08°	overall
Gof	6.71	6.22	5.82	3.93	1.31	5.46
$R(F)_{obs}$	3.21	3.72	3.92	3.90	1.38	
Rp	3.60	3.60	3.73	2.92	0.88	3.22
wRp	4.59	4.59	4.44	3.30	1.11	4.15

Table 3. Refined Magnetic Parameters

atom site	M_x (μ_B)	M_y (μ_B)	M_z (μ_B)
Mn/Co1	0	0	1.47(3)
Mn/Co2	0	0	−1.47(3)
Mn/Co3	0	0	1.47(3)

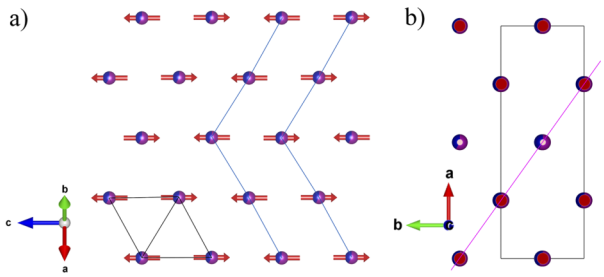

Figure 9. Schematic representation of the magnetic structure of PMCW; only the magnetic atoms are represented for clarity, a) the "fundamental unit" (black lines) and alternate zigzag stripes (blue line) of ferromagnetic interactions stacked in an AF way on the {111} plane of the fundamental perovskite; and b) orientation of the considered magnetic planes with respect to the magnetic cell.

structure, shown in Figure 9a, consists of four next neighbor magnetic atoms arranged in a triangular lattice with three almost equivalent distances ranging from 5.605(1) to 5.769(1) Å. If we consider the interactions generated by all the possible exchange paths, then they probably correspond to comparable energies with a main AF character. This is also confirmed by the presence of diffuse scattering above and below T_{C2}, which indicates that in spite of the fact that the Mn—Mn distances are not constrained to be the same by symmetry, the exchange interactions are probably comparable and compete with each other.[37−39] In this scenario, the system shows features of frustration. This would lead to the occurrence of degenerate configurations, but the observed symmetry reduction from $Pmcn1'$ to $Pm'c2_1'$ removes the degeneracy via a spin driven Jahn−Teller effect bringing small distortions.

Symmetry Analysis of the Long-Range Magnetic Transition. The mechanism of the releasing spin frustration through the structural distortions provides a natural explanation for the complex magnetic structure found experimentally below 9 K. The system combines the order parameters, mGM2+/mGM4−(ξ) and mY2(η_1,η_2), in order to couple the appropriate structural distortions which are the most efficient to lift the frustration. In particular, the presence of the two magnetic order parameters allows coupling a set of displacive modes with the Y2(δ_1,δ_2) symmetry via the trilinear free-energy term $\delta_2\xi\eta_1+\delta_1\xi\eta_2$ that simply turns into $\delta_2\xi\eta_1$ for the equilibrium conditions ($\eta_1 \neq 0$, $\eta_2 = 0$). These displacements apparently play the crucial role in the development of the magnetic ordering and the form of the invariant indicates that the coupling is maximal when both magnetic order parameters ξ and η_1 have the same values (the same size of the spin components with κ_1 = (0 0 0) and κ_2 = (1/2 0 0)). A precise determination of the dominant displacive modes with the Y2(0,δ_2) symmetry (out of 30 possible) are however beyond the resolution limit of the present powder diffraction experiment. The symmetry reduction at the long-range magnetic transition at T_{C2} turns the magnetic point group of the system from $mmm.1'$ to the acentric $m'm2'$, allowing the generation of a spontaneous electrical polarization, P, confirmed by the pyroelectric measurements (Figure 5). As pointed out above, the symmetry breaking is associated with the reducible magnetic order parameter mGM2+/mGM4−(ξ) ⊕ mY2($\eta_1 \neq 0$, $\eta_2 = 0$). The polar properties of PMCW, however, are imposed by the mY2 component solely, through the general free-energy invariant, $P(\eta_1^2 - \eta_2^2)$ which is reduced down to the simple product $P\eta_1^2$ for the equilibrium ordered parameter direction ($\eta_1 \neq 0$, $\eta_2 = 0$). This is a typical improper relationship between the polarization, transformed by the GM3- representation, and the κ_2 = (1/2 0 0) component of the magnetic order parameter, which implies the appropriate critical behavior.

The irreversibility between ZFC and FC measurements and the M(H) loop clearly indicate also that a weak ferromagnetic contribution, μ, is present in the system. Since the magnetic space group $Pm'c2_1'$ allows a ferromagnetic component along the ***b***-axis, the observed magnetic behavior can be associated with some spin-canting of the AF structure. This component possess the symmetry of the mGM2+(ξ) irreducible representation and therefore is bilinearly coupled ($\mu\xi$) to the primary antiferromagnetic configuration, through antisymmetric Dzyaloshinskii−Moriya exchange. Thus, the weak ferromagnetism and the electric polarization are induced by the different components of the magnetic order parameter (mGM2+, κ_1 = (0 0 0) and mY2, κ_2 = (1/2 0 0), respectively) and therefore are efficiently decoupled.

Modeling of the Induced Polarization. The temperature dependence of the polarization evaluated on the base of the linear-quadratic relation $P\eta_1^2$ is shown in the inset of Figure 10 compared with the integration of the pyrocurrent from 50 to 5 K. Clearly, the adopted model accounts in some extent for the experimental polarization below the long-range order transition.

DOI: 10.1021/acs.inorgchem.6b00117
Inorg. Chem. 2016, 55, 4381−4390

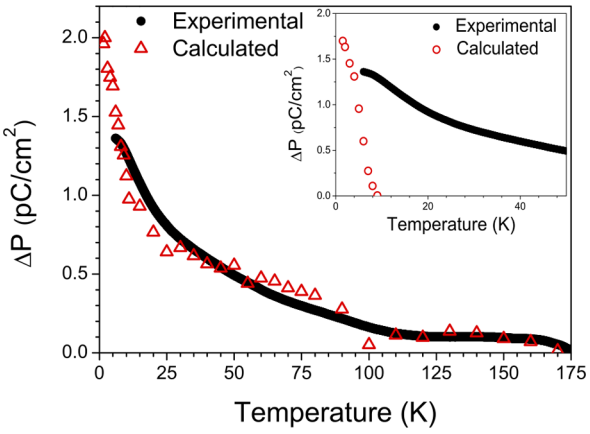

Figure 10. Experimental (black line) and calculated (red triangles) polarization as a function of temperature considering the short-range ordering in the sample (see text). Inset: the red circles indicate the magnetically induced polarization in the PMCW sample due to the sole long-range magnetic structure via the linear-quadratic free energy invariant.

This indicates that the improper polarization due to the long-range ordering represents one of the existing contributions to the macroscopic polarization at least. For temperatures higher than T_{C2} other contributions must be taken into account. The pyrocurrent measurements indicate a change of the system polarization also in correspondence with the short-range ordering transition at 188 K, and the hysteresis measurements point to this as the para-to-ferroelectric transition temperature. A possible mechanism is that the magnetic exchange interactions developing below T_{C1} generate local regions with a spontaneous electrical polarization, implying that the system may be inhomogeneous. These type of short-range ferroelectric distortions are already observed in literature,[41,42] generally resulting in relaxor properties. Oliveira et al. by using PDF analysis show the presence of local distortion in the $CdCr_2S_4$ compound, giving rise to the experimental observation of ferroelectric properties. Moreover, the authors show by susceptibility measurement and Landau theory the coupling of this short-range distortion with the magnetic properties of the system.[40]

The solid evidence for the presence of spin-driven electric polarization in the long-range ordered phase allows us to assume that a similar mechanism could be responsible for generating the polarization below T_{C1}. In this scenario the short-range magnetic interactions break locally the inversion center inducing the spontaneous polarization following the same free energy term relevant for the long-range magnetic structure. This is also consistent with the measurement of the ferroelectric hysteresis loop at 77 K that suggests the presence of two contributions: a pure dielectric one, generated by the paramagnetic regions, and a ferroelectric contribution induced by the short-range magnetically ordered regions.

In order to support this assumption, we model the experimental polarization using the evolution of the short-range magnetic interactions in the system. For this purpose, we integrated the paramagnetic background in the *d*-spacing range 14−18 Å (Figure 7), whose strong temperature dependence is an indication of the loss of pure paramagnetic regions, and as a consequence, of an increase of the short-range exchange interaction. Halpern and Johnson[42] have shown that the differential cross section of neutron due to a paramagnetic compound is as follows:

$$d\Phi_m = \frac{2}{3}S(S+1)\left(\frac{e^2\gamma F^{1/2}}{mc^2}\right)^2 d\Omega \quad (1)$$

where S is the spin quantum number, F is the amplitude of the form factor, γ is the neutron magnetic moment in μ_B, m is the mass of the neutron, e is the electric charge, and c is the speed of light.

If we assume that the major contribution to the variation of the background with temperature is due to the change in the magnetic behavior of the system, then the reduction of the paramagnetic background can be considered proportional to the increase of the fraction of interacting cations and in particular to $S(S+1)$ which is proportional to the order parameter. By taking this value from the experimental integration of the background and by using the free energy coupling term $P\eta_1^2$, it is possible to reproduce the temperature evolution of the experimental electrical polarization. The results are shown in Figure 10, where the calculated polarization has been scaled to take into account the unknown phenomenological constants. A good agreement, at least from a qualitative point of view, is clearly visible in spite of the quite simplified model irrespective of possible additional sources of electrical polarization. This suggests an important role of the symmetric exchange striction mechanism, confirming that the magnetic and electric ordering in the system are related by a spin−lattice interaction and that the frustration of the magnetic interaction is resolved via SDJT effect.

Finally, let us point out that in spite of the fact that within the resolution limit of our diffraction experiment, there is no evidence for structural changes at T_{C1}, a structural nature of this transition cannot be fully excluded. Some discontinuity in the bond valence sums of the cations concomitant with this transition indirectly supports the structural scenario. In this case, the symmetry change down to the polar structure of Pb_2MnWO_6 with the $Pmc2_11'$ space group is the main candidate to explain the presence of polarization below T_{C1}. The value of the polarization is, however, much smaller than in the Pb_2MnWO_6 counterpart, making it impossible to be detected in the present diffraction measurements.

CONCLUSIONS

In this paper, we identified a new type II multiferroic material $Pb_2Mn_{0.6}Co_{0.4}WO_6$. The system presents a centrosymmetric orthorhombic RT phase with s.g. *Pmcn1′*, with a full ordered double perovskite structure. The system undergoes a first magnetic transition at T_{C1} = 188 K, observed in the $M(T)$ measurements. The progressive increase of the applied magnetic field weakens this transition up to its complete suppression. No magnetic reflections appear in the ToF-NPD pattern being related to this transition, but the observed decrease of the paramagnetic background concomitant with an increase of diffuse scattering in the *d*-range 7−12 Å, indicates a development of short-range spin correlations. The transition is connected to the presence of a broad peak in the pyrocurrent measurement indication of the generation of spontaneous electrical polarization, and the DHM indicate a ferroelectric hysteresis loop with small saturation polarization. Because of the absence of antisite defects in the structure, this magnetic transition is probably ascribable to the magnetic interactions at the APB's.

DOI: 10.1021/acs.inorgchem.6b00117
Inorg. Chem. 2016, 55, 4381−4390

At 9 K, the pyrocurrent measurements show the generation, also in this case, of a spontaneous electrical polarization with the appearance of the long-range collinear antiferromagnetic ordering described by the noncentrosymmetric magnetic space group $Pm'c2_1'$. This transition is an example of a spin driven Jahn−Teller effect,[6−16] in which a small lattice distortion is induced to resolve the ground state degeneracy of a magnetically frustrated system. The observed polarization is produced by the breaking of the spatial inversion symmetry, and the polarization is coupled to the magnetic order parameter via the linear quadratic free energy term. The symmetry breaking mechanism observed at the long-range magnetic transition is likely transferable to the short-range magnetic transition at T_{C1} as supported by the modeling of the polarization trough the same free energy invariant. The magnetic symmetry and magnetization measurements both indicate the presence of spontaneous weak ferromagnetic moment. The ferroelectric polarization and the weak ferromagnetism, however, have been found to be associated with different components of the reducible magnetic order parameter and therefore are efficiently decoupled from each other.

■ ASSOCIATED CONTENT

Supporting Information

The Supporting Information is available free of charge on the ACS Publications website at DOI: 10.1021/acs.inorgchem.6b00117.

Tables with atomic coordinate and selected bond lengths and angles, Rietveld plots of additional data, thermal evolution of bond lengths, magnetic symmetry analysis results, and electrical measurements (PDF)
CIF files (CIF)
mCIF files (mCIF)

■ AUTHOR INFORMATION

Corresponding Author

*E-mail: fabio.orlandi@stfc.ac.uk (F.O.).

Author Contributions

The manuscript was written through contributions of all authors. All authors have given approval to the final version of the manuscript.

Notes

The authors declare no competing financial interest.

■ ACKNOWLEDGMENTS

F.O. thanks Fondazione Cariparma for financial support. The authors acknowledge the STFC for the provision on neutron beamtime and the ESRF institute for the provision of the synchrotron light. The authors thank Dr. Jessica Hudspeth for the help during the synchrotron experiment.

■ REFERENCES

(1) Khomskii, D. *Physics* **2009**, *2*, 20.
(2) Bersuker, I. B. *Phys. Rev. Lett.* **2012**, *108*, 137202.
(3) Catalan, G.; Scott, J. F. *Adv. Mater.* **2009**, *21*, 2463−2485.
(4) Tokura, Y.; Shinichiro, S.; Nagaosa, N. *Rep. Prog. Phys.* **2014**, *77*, 076501.
(5) Cheong, S. W.; Mostovoy, M. *Nat. Mater.* **2007**, *6*, 13−20.
(6) Yamashita, Y.; Ueda, K. *Phys. Rev. Lett.* **2000**, *85*, 4960−4963.
(7) Lorenz, B.; Wang, Y.; Chu, C. W. *Phys. Rev. B: Condens. Matter Mater. Phys.* **2007**, *76*, 104405.
(8) Sergienko, I. A.; Sen, C.; Dagotto, E. *Phys. Rev. Lett.* **2006**, *97*, 227204.
(9) Lee, N.; Choi, Y. J.; Ramazanoglu, M.; Ratcliff, W., II; Kiryukhin, V.; Cheong, S.-W. *Phys. Rev. B: Condens. Matter Mater. Phys.* **2011**, *84*, 020101R.
(10) Radaelli, P. G.; Chapon, L. C. *J. Phys.: Condens. Matter* **2008**, *20*, 434213.
(11) Noda, Y.; Kimura, H.; Fukunaga, M.; Kobayashi, S.; Kagomiya, I.; Kohn, K. *J. Phys.: Condens. Matter* **2008**, *20*, 434206.
(12) Hur, N.; Park, S.; Sharma, P. A.; Ahn, J. S.; Guha, S.; Cheong, S.-W. *Nature* **2004**, *429*, 392−395.
(13) Hur, N.; Park, S.; Sharma, P. A.; Guha, S.; Cheong, S.-W. *Phys. Rev. Lett.* **2004**, *93*, 107207.
(14) Blake, G. R.; Chapon, L. C.; Radaelli, P. G.; Park, S.; Hur, N.; Cheong, S.-W.; Rodríguez-Carvajal. *Phys. Rev. B: Condens. Matter Mater. Phys.* **2005**, *71*, 214402.
(15) Chapon, L. C.; Blake, G. R.; Gutmann, M. J.; Park, S.; Hur, N.; Radaelli, P. G.; Cheong, S.-W. *Phys. Rev. Lett.* **2004**, *93*, 177402.
(16) Chapon, L. C.; Radaelli, P. G.; Blake, G. R.; Park, S.; Cheong, S.-W. *Phys. Rev. Lett.* **2006**, *96*, 097601.
(17) Orlandi, F.; Righi, L.; Cabassi, R.; Delmonte, D.; Pernechele, C.; Bolzoni, F.; Mezzadri, F.; Solzi, M.; Merlini, M.; Calestani, G. *Inorg. Chem.* **2014**, *53*, 10283−10290.
(18) Chapon, L. C.; Manuel, P.; Radaelli, P. G.; Benson, C.; Perott, L.; Ansell, S.; Rhodes, N. J.; Raspino, D.; Duxbury, D.; Spill, E.; Norris, J. *Neutron News* **2011**, *22*, 22−25.
(19) Petricek, V.; Dusek, M.; Palatinus, L. *Z. Kristallogr. - Cryst. Mater.* **2014**, *229*, 345−352.
(20) Campbell, B. J.; Stokes, H. T.; Tanner, D. E.; Hatch, D. M. *J. Appl. Crystallogr.* **2006**, *39*, 607−614.
(21) Cabassi, R.; Bolzoni, F.; Gauzzi, A.; Gilioli, E.; Prodi, A.; Licci, F. *Phys. Rev. B: Condens. Matter Mater. Phys.* **2006**, *74*, 045212.
(22) Baldinozzi, G.; Sciau, Ph.; Pinot, M.; Grebille, D. *Acta Crystallogr., Sect. B: Struct. Sci.* **1995**, *51*, 668−673.
(23) Nespolo, M.; Ferraris, G.; Ohashi, H. *Acta Crystallogr., Sect. B: Struct. Sci.* **1999**, *55*, 902−916.
(24) Walsh, A.; Payne, D. J.; Egdell, R. G.; Watson, G. W. *Chem. Soc. Rev.* **2011**, *40*, 4455−4463.
(25) Shirane, G.; Pepinsky, R.; Frazer, B. C. *Acta Crystallogr.* **1956**, *9*, 131−140.
(26) Halasyamani, P. S. *Chem. Mater.* **2004**, *16*, 3586−3592.
(27) Mandal, T. K.; Abakumov, A. M.; Lobanov, M. V.; Croft, M.; Poltavets, V. V.; Greenblatt, M. *Chem. Mater.* **2008**, *20*, 4653−4660.
(28) Blanco, M. C.; De Paoli, J. M.; Ceppi, S.; Tirao, G.; Nassif, V. M.; Guimpel, J.; Carbonio, R. E. *J. Alloys Compd.* **2014**, *606*, 139−148.
(29) Viola, M. C.; Martınez-Lope, M. J.; Alonso, J. A.; Martınez, J. L.; De Paoli, J. M.; Pagola, S.; Pedregosa, J. C.; Fernandez-Dıaz, M. T.; Carbonio, R. E. *Chem. Mater.* **2003**, *15*, 1655−1663.
(30) Orlandi, F.; Righi, L.; Ritter, C.; Pernechele, C.; Solzi, M.; Cabassi, R.; Bolzoni, F.; Calestani, G. *J. Mater. Chem. C* **2014**, *2*, 9215−9223.
(31) Senn, M. S.; Arevalo-Lopez, A. M.; Saito, T.; Shimakawa, Y.; Attfield, J. P. *J. Phys.: Condens. Matter* **2013**, *25*, 496008.
(32) Rodríguez-Carvajal, J. *Phys. B* **1993**, *192*, 55−69.
(33) Gallego, S. V.; Tasci, E. S.; de la Flor, G.; Perez-Mato, J. M.; Aroyo, M. I. *J. Appl. Crystallogr.* **2012**, *45*, 1236−1247.
(34) Aroyo, M. I.; Perez-Mato, J. M.; Orobengoa, D.; Tasci, E.; de la Flor, G.; Kirov, A. *Bulg. Chem. Commun.* **2011**, *432*, 183−197.
(35) Aroyo, M. I.; Perez-Mato, J. M.; Capillas, C.; Kroumova, E.; Ivantchev, E.; Madariaga, G.; Kirov, A.; Wondratschek, H. *Z. Kristallogr. - Cryst. Mater.* **2006**, *221*, 15−27.
(36) Aroyo, M. I.; Kirov, A.; Capillas, C.; Perez-Mato, J. M.; Wondratschek, H. *Acta Crystallogr., Sect. A: Found. Crystallogr.* **2006**, *62*, 115−128.
(37) Manuel, P.; Chapon, L. C.; Radaelli, P. G.; Zheng, H.; Mitchell, J. F. *Phys. Rev. Lett.* **2009**, *103*, 037202.
(38) Khalyavin, D. D.; Manuel, P.; Mitchell, J. F.; Chapon, L. C. *Phys. Rev. B: Condens. Matter Mater. Phys.* **2010**, *82*, 094401.

DOI: 10.1021/acs.inorgchem.6b00117
Inorg. Chem. 2016, 55, 4381−4390

(39) Khalyavin, D. D.; Manuel, P.; Ouladdiaf, B.; Huq, A.; Stephens, P. W.; Zheng, H.; Mitchell, J. F.; Chapon, L. C. *Phys. Rev. B: Condens. Matter Mater. Phys.* **2011**, *83*, 094412.
(40) Oliveira, G. N. P.; Pereira, A. M.; Lopes, A. M. L.; Amaral, J. S.; dos Santos, A. M.; Ren, Y.; Mendonça, T. M.; Sousa, C. T.; Amaral, V. S.; Correia, J. G.; Araújo, J. P. *Phys. Rev. B: Condens. Matter Mater. Phys.* **2012**, *86*, 224418.
(41) Ramesha, K.; Llobet, A.; Proffen Th; Serrao, C. R.; Rao, C. N. R. *J. Phys.: Condens. Matter* **2007**, *19*, 102202.
(42) Halpern, O.; Johnson, M. H. *Phys. Rev.* **1939**, *55*, 898.

DOI: 10.1021/acs.inorgchem.6b00117
Inorg. Chem. 2016, 55, 4381−4390